RESEARCH PAPER

Metamodeling-based parametric optimization of DBD plasma actuation to suppress flow separation over a wind turbine airfoil model

Ramsankar Veerakumar[1] · Vishal Raul[1] · Yang Liu[1] · Xiaodong Wang[2] · Leifur Leifsson[1] · Hui Hu[1]

Abstract

While dielectric-barrier-discharge (DBD) based plasma actuation systems have been successfully demonstrated to suppress massive flow separation over wind turbine blades to reduce the transient aerodynamic loadings acting on the turbine blades, it is still a non-trivial task to establish a best combination of various operating parameters for a DBD plasma actuation system to achieve the optimized flow control effectiveness. In the present study, a regression Kriging based metamodeling technique is developed to optimize the operating parameters of a DBD plasma actuation system for suppressing deep stall over the surface of a wind turbine blade section/airfoil model. The data points were experimentally obtained by embedding a nanosecond-pulsed DBD (NS-DBD) plasma actuator at the leading edge of the airfoil model. The applied voltage and frequency for the NS-DBD plasma actuation were used as the design variables to demonstrate the optimization procedure. The highest possible lift coefficient of the turbine airfoil model at deep stalled angles of attack (i.e., $\alpha = 22°$ and $24°$) were selected as the objective function for the optimization. It was found that, while the metamodeling-based procedure could accurately predict the objective function within the bounds of the design variables with an uncertainty $\sim 2\%$, a global accuracy level of $\sim 97\%$ was achieved within the whole design space.

1 Introduction

Wind energy industry is currently undergoing a period of rapid growth on a global scale fueled by increasingly stringent norms on the utilization of conventional fossil fuels for power production. For instance, the U.S. Department of Energy (DOE) initiated the *Wind Vision* study where the costs and benefits of continued investments on wind energy was quantified. The study evaluates an ambitious, yet credible scenario in which wind energy will serve 20% of the nation's total electric power demand by 2030, and 35% by 2050 [1]. Other countries have increased their wind power capacity as well in recent years. For example, wind power installation in China has been growing recently by an annual rate of $\sim 10\%$ until 2020 [2].

Attempts to extract more energy from the wind has led to bigger and bigger rotor diameters of wind turbines. While turbine rotor diameters of ~ 120 meters is quite common today, one of the major challenges faced by large-scale wind turbines is the constant variations in the direction and speed of the turbulent atmospheric boundary layer (ABL) winds which the turbines are exposed to. The ability of a wind turbine to respond to the rapid fluctuations of ABL winds in both speed and direction is hindered by the massive rotational inertia of the large-scale turbine assembly as a whole. Thus, wind turbine blades often operate under less than optimal conditions in relation to the instantaneous ABL wind speeds and directions [3]. The highly turbulent nature of the ABL winds would induce unsteady wind loadings acting on the turbine blades, which has become a severe problem with larger rotor diameters. If the unsteady wind loads can be reduced to a lower level, it will lead to a lighter structure and longer fatigue lifetime of the turbine blades, thereby, better economics of power production [4]. Experimental investiga-

✉ Hui Hu
huhui@iastate.edu

1 Department of Aerospace Engineering, Iowa State University, Ames, IA 50010, USA

2 School of Energy, Power and Mechanical Engineering, North China Electric Power University, Beijing, China

tions to understand the effects of incoming surface wind on the turbine wake and the wake interference among upstream and downstream wind turbines has been conducted in the past [5]. Mitigating the unsteady wind loads acting on a turbine blade, could be realized by using various flow control methods, including mechanically operated flaps or adding momentum to the flow at specific locations on the turbine blades [6]. For example, van Dam et al. [7] suggested to utilize trailing edge flaps to control flow separation over turbine blades. While the use of trailing edge flaps has been revealed to be effective in providing unsteady wind load mitigation, the major disadvantage of such a method is the mechanical complexity, added mass, and additional maintenance requirements. Such drawbacks could be avoided if the flow control devices devoid of moving parts could be used instead. Plasma-based flow control approach has been suggested to be a potential solution for flow separation control to mitigate the unsteady wind loadings acting on wind turbine blades [8].

Roth et al. [9] are among the first to report that dielectric-barrier-discharge (DBD) plasma actuation would have favorable effects on flow control about two decades ago. Since then, numerous studies have been conducted to employ DBD plasma actuation for various flow control applications [10–16]. Plasma based flow control is still an actively pursued area of research and finds applications on airfoils, as well as road vehicles [17–22] Plasma based flow control technique has several advantages in comparison to other traditional techniques used for active flow control. It does not involve any moving parts which significantly reduces the mechanical wear and tear. The response time of DBD plasma activation is very short and it instantaneously activates when triggered with the high voltage pulses [14]. DBD plasma actuators can be surface mounted and require lower electrical power for the flow control operations [23]. Due to relatively simple system setup for DBD plasma generation, DBD plasma actuators can also be incorporated into existing structures easily.

Figure 1 shows the schematic of a typical DBD plasma actuator used for flow control. As shown in the figure, a dielectric layer is sandwiched between two metal electrodes and the whole system can then be flush mounted to the surface over which the flow control is desired. The material used as the dielectric layer is typically an electrical insulator, such as Teflon, Kapton, Poly-Vinyl Chloride (PVC), glass, ceramic or Plexiglas. The air close to the electrode would get ionized and creates the surface plasma when high voltages are applied to the exposed electrode with the other (encapsulated) electrode electrically grounded. DBD plasma actuation has been found to modify the flow fields over airfoil surfaces favorably under controlled conditions when operated within a range of Reynolds number and angles of attack [10–16].

Alternating current based dielectric barrier discharge (i.e., AC-DBD) plasma and nano-second based dielectric barrier
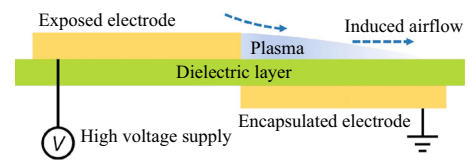

Fig. 1 Schematic diagram of a DBD plasma actuator

discharge (i.e., NS-DBD) plasma are two most commonly used DBD plasma configurations used for flow control studies. AC-DBD plasma, activated by an alternating current at relatively high voltages (typically about 10–30 kV) has been found to be able to induce an ionic wind in quiescent conditions with flow velocities typically of the order of 4–7 m/s [15, 24]. This induced velocity is primarily responsible for the flow separation control. In the case of NS-DBD plasma, intermittent high voltage pulses at some predefined frequency are applied with pulse rise times lasting for only a few nanoseconds as opposed to the continuous sinusoidally varying alternating currents in AC-DBD plasma generation. While NS-DBD plasma actuation induces lower momentum effects in comparison to AC-DBD plasma [13], it was found to exhibit a superior flow control performance due to the rapid deposition of energy by the short plasma pulses to cause steep thermal gradients in the localized area. The fast thermalization of NS-DBD plasma has also found to induce a shock wave and associated secondary vortex which will interact with the main flow by exciting the inherent flow instabilities to augment the flow control effects [12, 13, 25].

While majority of the previous studies of plasma-based flow control focused on suppression flow separation over the surfaces of airfoil/wing models designed for aeronautical applications, only limited attempts can be found in literature to apply plasma-based technique to control flow separation or/and airfoil stall for wind turbine applications. Nelson et al. [8] proposed a novel smart wind turbine blade concept, where the effectiveness of plasma-based flow control was exploited. The regions over the wind turbine blades requiring individual control could be identified and mounted with DBD plasma actuators and separate control strategies could be devised to meet multiple control objectives. More recently, Hikaru et al. [26] investigated numerically the effectiveness of active flow control using plasma actuators on NREL S825 wind turbine airfoil. They reported that, by turning on the DBD plasma actuator, a partial reattachment was realized and the lift-to-drag ratio was found to increase from 2.24 to 6.53.

It should be noted that, there are a number of operating parameters (design variables) involved in a well-designed DBD plasma actuator, including the applied voltage and frequency of the activation, the width of the exposed and encapsulated electrodes, the material and thickness of the dielectric layer. Forte et al. [15] conducted a comprehensive investigation on the effects of all the important design

variables for an AC-DBD plasma actuator by varying one parameter at a time, while the others remained constant. Dawson et al. [13] also conducted a similar study for NS-DBD plasma actuation. While these previous studies have contributed immensely to a better understanding about plasma-based flow control techniques, only a small fraction of the entire parametric design space was explored due to the inherent nature of varying only a parameter at a time. The cost of the experiments can severely limit the optimization and design space exploration.

Use of metamodel-based optimization technique could be a solution to this problem. Metamodeling techniques are generally used to for parametric optimization when conducting simulations or experiments to explore the entire design space is very expensive [27, 28]. Metamodeling-based optimization techniques allow multiple design variables to be simultaneously varied and have been applied to several expensive parametric optimization studies in recent years, including rotor blade design and optimization [29], high speed civil transport [30], airfoil shape optimization [31], diffuser shape optimization [32] and supersonic turbine [33, 34]. Kriging is one of the most popularly used metamodeling techniques [35]. Kriging metamodels could be based on an interpolating scheme or a regression scheme. Interpolating scheme would ensure that the model passes through all the sample data points. While a noisy data resulting from an experimental error could affect the prediction accuracy of the interpolation Kriging metamodel, the random error in physical experiments lends itself to the use of a regression model as a noise filter which would not restrict the model to go through all the points [35].

In the present study, we report the progress made in our recent efforts to conduct a parametric optimization of design variables of DBD plasma actuation using a metamodeling-based technique in order to suppress the massive flow separation over the surface of a wind turbine airfoil in deep stall. A turbine blade model with DU-96-W-180 airfoil shape in cross-section was designed and manufactured for the present study. A DBD plasma actuator working in nanosecond mode (i.e., NS-DBD) was embedded at the leading edge of the turbine airfoil model for flow separation control. The parameters of interest (design variables) used in the present study are the applied voltage and frequency of the NS-DBD plasma pulses. The turbine airfoil model was mounted in a low-speed wind tunnel at the angle of attack of $\alpha = 24°$ with a chord-based Reynolds number of $Re = 200 \times 10^3$. The objective of the present study is to find the optimum combination of these design variables of the NS-DBD plasma actuation for maximizing the lift coefficient (C_l) of the turbine airfoil model at the given angle of attack. The design variables are simultaneously varied in the design space as per a sampling scheme obtained using the Latin hyper cube (LHS) sampling technique. The turbine airfoil

model was also subjected to a different Reynold number and angle of attack (i.e., with the Reynolds number of $Re = 300 \times 10^3$ and $\alpha = 22°$) in order to verify the effects of Reynolds number and the angle of attack on the optimum parameters. The data points used for the optimization procedure were obtained experimentally by integrating the measured surface pressure distributions over the wind turbine airfoil model to obtain the lift coefficients (C_l). These C_l values obtained served as evaluated objective function values at the initial sample locations for the metamodel. A digital Particle Image Velocimetry (PIV) system was also used in the present study to quantify the airflow field over the airfoil surface for the selected cases.

It should be noted that, while a wide variety of previous studies have been conducted on DBD plasma-based flow control, parametric optimization of DBD plasma actuation using the metamodeling-based technique has never been attempted. To the best of authors' knowledge, this is the first attempt to combine experimental measurements with metamodeling-based techniques in order to establish the best combination of various operating parameters (design variables) of a DBD plasma actuation system. The present study aims to demonstrate that parametric optimization of the whole design space could be accomplished with lesser number of sample data points and yet maintain reasonable accuracy of prediction of the objective function within the bounds of design variables. Such metamodeling based techniques could drastically reduce the number of experiments required for characterizing the whole design space.

2 Problem definition for the optimization

The present study utilizes a metamodel-based optimization technique to estimate the optimum values of the applied voltage and frequency of a NS-DBD plasma system for obtaining the maximum lift coefficient (C_l) of a turbine airfoil operating in deep stall condition. An increase in the C_l of the turbine airfoil model is an indicator of improvement in partial reattachment of the separated flow over the airfoil surface. Since surface pressure measurements are acquired during the experiments, the objective function of the present study is seeking the maximum possible C_l, ($C_{l\max}$) and the combination of design variables which could achieve that value. The bounds on the design variables were decided based on previous experiments using a similar configuration. It was observed that applied voltages to the DBD plasma actuator in excess of 17 kV tends to burn through the dielectric layer (i.e., for the given dielectric layer used in the present study). The frequency of the applied voltage pulses exceeding 500 Hz and lower than 10 Hz did not seem to have any effects on the flow separation over the airfoil surface. Accordingly, the applied voltage was varied between 5.0 kV to 14.0 kV, and

the range of frequency of the applied voltage pulses was set to be within 10 Hz to 500 Hz which are the bounds of the design variables used here.

Thus, the optimization problem is formulated as:

$$\min_{\mathbf{x}} F(\mathbf{x}) = -C_l,$$

$$\text{s.t.} \mathbf{x}_{lb} \le \mathbf{x} \le \mathbf{x}_{ub}. \tag{1}$$

Here, $F(\mathbf{x})$ represent objective or cost function with $\mathbf{x} = [V f]^{\mathrm{T}}$ is a column vector with voltage and frequency as the design variables. The negative sign is used for maximizing objective function with minimization optimizer. The objective function is subjected to design variable bounds $\mathbf{x}_{lb} \le \mathbf{x} \le \mathbf{x}_{ub}$, where $\mathbf{x}_{lb} = [5\,1\,0]^{\mathrm{T}}$ and $\mathbf{x}_{ub} = [14\,500]^{\mathrm{T}}$ are the lower and upper bounds for design variable vector, respectively.

For comparing the effectiveness of DBD plasma actuation on improving the lift coefficient of the turbine airfoil model, the baseline lift coefficient for the test case with a passive actuator was used. The test case with the passive actuator refers to the scenario with the DBD plasma actuator being mounted at the airfoil leading edge but without turning the plasma actuators on.

3 Experimental setup and test model

3.1 Wind tunnel used for the present study

The experimental study was performed at a low-speed, closed-circuit wind tunnel located at Aerospace Engineering Department of Iowa State University. The tunnel has a test section with a dimension of 0.45 m × 0.6 m × 1.45 m (width × height × length) and four optically transparent walls. It has a relatively large contraction section (i.e., 10:1 in area ratio) upstream of the test section along with series of honeycomb, screen structures, and cooling system installed ahead of the contraction section to provide uniform, low turbulent incoming flow to enter the test section. The maximum airflow speed in the test section can go up to 40 m/s with the turbulence intensity level being 0.2%, as measured using a hotwire anemometer.

3.2 Wind turbine airfoil model used for the present study

As shown schematically in Fig. 2, a wind turbine blade section model with DU-96-W-180 airfoil shape in the cross section was designed and manufactured for the present experimental study. The DU-96-W-180 airfoil, which is a cambered airfoil with a blunt trailing edge and a maximum thickness of 18% chord length, is a widely-used airfoil
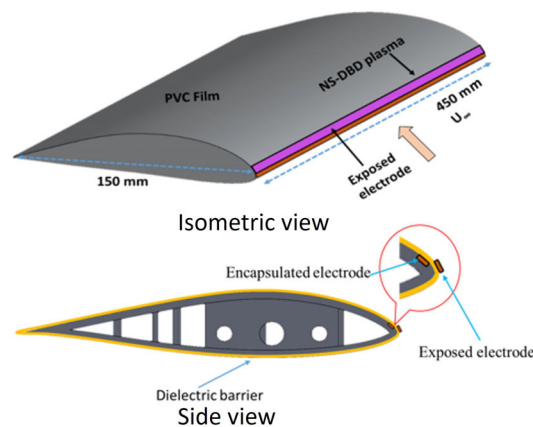
(a) Schematic diagram of the turbine airfoil model embedded with the DBD plasma actuator
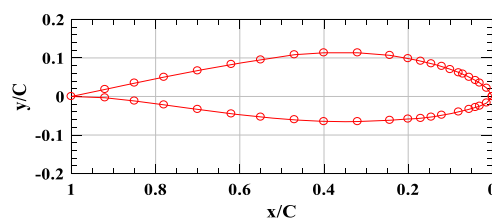
(b) Distribution of pressure taps around the airfoil model

Fig. 2 Schematic diagram of the turbine airfoil model with a NS-DBD plasma actuator embedded at the airfoil leading edge

designed specifically for wind turbine applications [36]. The airfoil shape is known for its favorable aerodynamic performance and strong structural strength, which are very important for wind turbine blades. The turbine airfoil model has a chord length of $C = 150$ mm and spanwise length of 600 mm (i.e., the same as the width of the wind tunnel test section). It was manufactured by using a rapid prototyping machine (i.e., 3D printer) with a polymer-composite-based material. The surface of the turbine airfoil model was coated with several layers of spray-on primer, and wet-sanded by using fine sandpapers (up to 2000 grit) to achieve a very smooth, glossy surface finish with ~ 20 μm in surface roughness. As shown in Fig. 2b, 42 pressure taps were incorporated in the design of the airfoil model.

3.3 NS-DBD plasma actuator

A DBD plasma actuator was embedded around the leading edge of the airfoil model, as shown schematically in Fig. 2a. Both the encapsulated and exposed electrode had a width of 3.0 mm and was made of ~ 100 μm thick copper film. The electrodes cover the entire span of the turbine airfoil model to ensure a spanwise uniform plasma formation to prevent any three dimensional effects. A layer of PVC film, ~ 300 μm in thickness was used as the dielectric layer.
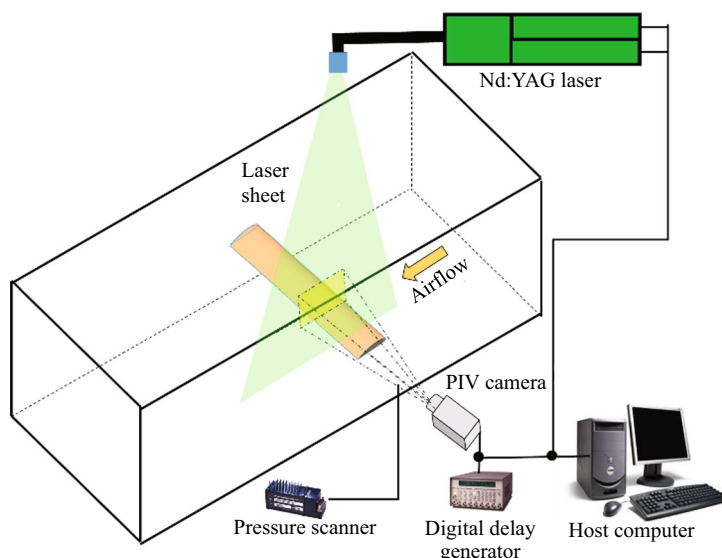
Fig. 3 Schematic diagram of the experimental setup used in the present study

The DBD plasma actuator was powered by using high voltage pulses with a FID nanosecond pulse generator (FPG 20-10NM15), which has the capability to generate pulses up to 20 kV voltage (i.e., ~ 20 ns in pulse width) and pulse repetition frequency (PRF) up to 10 kHz. The applied voltage and current pulses were monitored by using a Tektronix MDO3102 Mixed Domain Oscilloscope with 5 GSa/s sampling rate. It should be noted that, NS-DBD plasma actuation could create electromagnetic interference (EMI) effects to nearby electronic components. The EMI effects were mitigated by proper grounding of all equipment and covering the test section and all the electronic components and cables with a curtain of conductive metallic fabric.

3.4 Surface pressure measurements

As shown in Fig. 2b, 42 pressure taps were arranged in the mid-section of the turbine airfoil model to measure the surface pressure distribution around the airfoil surface. The pressure taps were connected to two units of miniature digital pressure scanners (Measurement Specialties Inc, Model number 32HD-0411021120, 32 channels per unit) with Tygon tubing of 1.5 mm diameter and 0.5 m length. The miniature digital pressure scanners incorporate temperature-compensated piezo-resistive pressure sensors with a pneumatic calibration valve, RAM, 16bit A/D converter, and a microprocessor in a compact self-contained module. The precision of the pressure acquisition system is ± 0.03% of the ± 10 inch H_2O full scale range (1 inch = 25.4 mm). During the experiments, the instantaneous surface pressure measurement data were acquired for 10 s at a data acquisition rate of 1000 Hz. It should also be noted

that, since the exposed electrode of the DBD plasma actuator (~ 100 µm in thickness) was placed at the leading edge of the airfoil model, it would cover a few pressure taps near the airfoil leading edge on the suction side. The surface pressure values at these locations will be obtained by extrapolating the surface pressure values measured at the neighbors taps. Similar extrapolation schemes were widely used in similar studies with plasma flow control [23].

3.5 Particle image velocimetry (PIV) measurements

In addition to the surface pressure measurements, a digital particle image velocimetry (PIV) system was also used to conduct airflow field measurements to quantify the changes of the flow characteristics around the airfoil model with and without the NS-DBD plasma actuation. As shown schematically in Fig. 3, the PIV measurements were conducted in the vertical planes near the mid-section of the airfoil model (i.e., slightly away from the middle plane with the pressure taps). For the PIV measurements, the oncoming airflow was seeded with 1–5 µm oil droplets by using a seeding generator. Illumination was provided by a double-pulsed Nd:YAG laser (Evergreen, Big Sky Laser) adjusted on the second harmonic and emitting two pulses of 200 mJ at the wavelength of 532 nm with a repetition rate of 10 Hz. The laser beam was shaped to a thin sheet by a set of mirrors, spherical, and cylindrical lenses. The thickness of the laser sheet in the measurement region was about 1.0 mm. A high-resolution 12-bit digital camera (2048 pixel by 2048 pixel resolution, PCO-Tech) with a Nikon Nikkor 60 mm 1:2.8 D lens was used to acquire images of tracer particles for the PIV measurements. The digital camera and the double-pulsed Nd:YAG
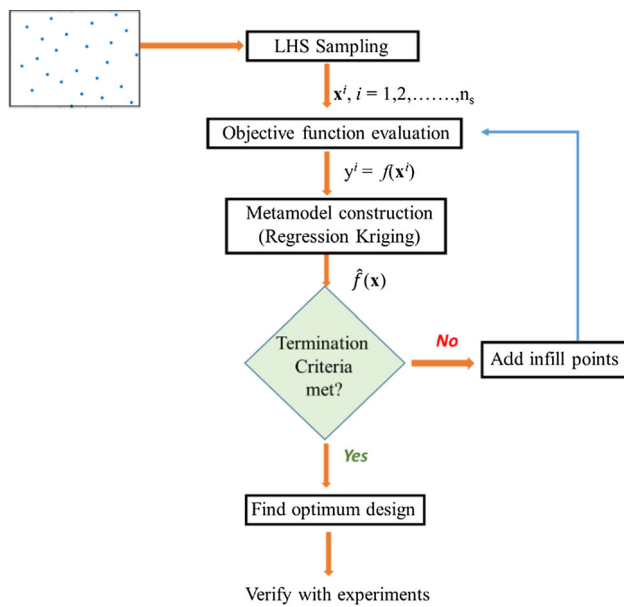
Fig. 4 Flowchart of the metamodeling procedure

lasers were connected to a workstation (host computer) via a Digital Delay Generator (Berkeley Nucleonics, Model 565), which controlled the timing of the laser illumination and the image acquisition for the PIV measurements.

After acquiring the PIV images, instantaneous velocity vectors were obtained by frame to frame cross-correlation of the patterns of particle images, using an interrogation window size of 32 pixels × 32 pixels. An effective overlap of 50% of the interrogation windows was employed in PIV image processing. In the present study, a cinema sequence of about 300 instantaneous PIV measurements were used to calculate the ensemble-averaged flow field around the airfoil model for the test cases with and without the NS-DBD actuation. The measurement uncertainty level for the instantaneous PIV measurements is estimated to be within 5.0%, while the uncertainty level for the measurements of the ensemble-averaged flow field being about 3.0%.

4 Metamodeling-based optimization

4.1 Optimization algorithm

Figure 4 shows the flowchart of the optimization algorithm which subsequently improves metamodel with infill criteria. The details of the optimization algorithm are explained below.

The optimization algorithm starts with generation of initial samples in design domain. Latin Hypercube sampling (LHS) technique is used for generating initial design samples ($\mathbf{x}^1, \mathbf{x}^2, \ldots, \mathbf{x}^{n_s}$), where $\mathbf{x}^i$ represents ith sample in total

n_s design samples. For this study, voltage and frequency are considered as design variables as mentioned earlier. LHS method ensures the good distribution of sampling points over the entire design space such that entire range of each design variable is covered. This is done by dividing considered cumulative probability distribution [0 to 1] of points in equal parts and randomly sampling each interval to recreate input probability distribution [37]. Additionally, to ensure space fillingness property of the design space, the Morris-Mitchell criterion is used. More details on this scheme is given by Morris and Mitchell [38].

One of the challenges of surrogate based optimization study is to decide required number of initial samples for accurate construction of metamodel. Having higher number of samples are always preferred for ensuring metamodel accuracy. However, in the present study, 12 samples per design variable are selected as initial sampling plan considering high cost of experimental evaluation of objective function (i.e., for two design variables, applied voltage and frequency, 24 sample points were used).

4.2 Regression Kriging

The surrogate based optimization techniques are widely used in field of optimization especially when objective function evaluation is expensive. In this technique an approximate cost function of expensive experiments are constructed which then is used in conjunction with a global optimizer to find optimum result. Kriging is a popular geostatistical technique which has been extensively used for multidisciplinary design and optimization studies [25]. Kriging method is named after the pioneering work of Krige [39], which was formally developed by Matheron [40]. Kriging method (interpolation kriging) generally assumes that the objective function value evaluated at sample points, which is used for generating the metamodel, does not have an error and represents true value. This method is capable of capturing complex multi-modal landscape of the objective function. However, when the method is presented with noisy data, as that obtained from experiments, it could produce incorrect global optimum. In such cases regression Kriging method which extracts a smooth trend from the data and filters noise is preferred [35].

Regression Kriging method is primarily an extension of the interpolation Kriging method. The interpolation Kriging method is hereafter called as Kriging method. Therefore, first the Kriging method is presented. Later the modifications to handle noisy data is addressed through regression Kriging method. Kriging model start with set of sample data n_s observed at initial sampling plan obtained by LHS method. Kriging metamodel is built as a combination of a global approximation function plus a localized departure as

$$y(\mathbf{x}) = g(\mathbf{x}) + Z(\mathbf{x}), \tag{2}$$

where $y(\mathbf{x})$ is the unknown function sought and $Z(\mathbf{x})$ is realization of a normally distributed Gaussian random process with zero mean, variance σ^2 and nonzero covariance [27]. Function $g(\mathbf{x})$ is a global approximation of the design space and $Z(\mathbf{x})$ represents the localized deviations from global function over design domain with n_s sampled data points $(\mathbf{x}^1, \mathbf{x}^2, \ldots, \mathbf{x}^{n_s})$ where $\mathbf{x}^i = [x_1, x_2, \ldots, x_K]^{\mathrm{T}} \subset \mathbb{R}^K$. Function $Z(\mathbf{x})$ has a covariance matrix given by

$$Cov\left[Z\left(\mathbf{x}^i\right), Z\left(\mathbf{x}^j\right)\right] = \sigma^2 \mathbf{R}\left(\left[R\left(\mathbf{x}^i, \mathbf{x}^{j)}\right)\right]\right), \tag{3}$$

where $\mathbf{R}$ represents the correlation matrix and $R(\mathbf{x}^i, \mathbf{x}^j)$ is a correlation function between any two sampled data points $\mathbf{x}^i$ and $\mathbf{x}^j$. This makes $\mathbf{R}$ a (n_s, n_s) symmetric matrix with ones along the diagonal. The correlation function R is a user defined function and for this study we have used Gaussian correlation function of the form

$$R\left(\mathbf{x}^i, \mathbf{x}^j\right) = \exp\left[-\sum_{k=1}^{K} \theta_k \left|x_k^i - x_k^j\right|^2\right], \tag{4}$$

where θ_k represents the unknown correlation parameters which determines shape of gaussian correlation function and x_k^i and x_k^j represents kth component of any two sample points $\mathbf{x}^i$ and $\mathbf{x}^j$.

Predicted estimates of the function sought at the unsampled points are given by

$$\hat{y}(\mathbf{x}_u) = \hat{\beta} + \mathbf{r}^{\mathrm{T}}(\mathbf{x}_u)\mathbf{R}^{-1}\left(\mathbf{y} - g\hat{\beta}\right), \tag{5}$$

where $\mathbf{y}$ is a column vector of length n_s which holds the sample values of the response. Function g is a column vector of similar length filled with ones when $g(\mathbf{x})$ is considered constant. The function $\mathbf{r}^{\mathrm{T}}(\mathbf{x}_u)$ is the correlation vector of length n_s between an untried $\mathbf{x}_u$ and the sampled data points $(\mathbf{x}^1, \mathbf{x}^2, \ldots, \mathbf{x}^{n_s})$ given by

$$\mathbf{r}^{\mathrm{T}}(\mathbf{x}_u) = \left[R\left(\mathbf{x}_u, \mathbf{x}^1\right), R\left(\mathbf{x}_u, \mathbf{x}^2\right), \ldots R\left(\mathbf{x}_u, \mathbf{x}^{n_s}\right)\right]^{\mathrm{T}}, \tag{6}$$

and $\hat{\beta}$ is estimated as

$$\hat{\beta} = (g^{\mathrm{T}}\mathbf{R}^{-1}g)^{-1}g^{\mathrm{T}}\mathbf{R}^{-1}\mathbf{y}. \tag{7}$$

Variance between the underlying global model with $\hat{\beta}$ and $\mathbf{y}$ is evaluated as

$$\hat{\sigma}^2 = \left[\left(\mathbf{y} - g\hat{\beta}\right)^{\mathrm{T}}\mathbf{R}^{-1}\left(\mathbf{y} - g\hat{\beta}\right)\right] \Big/ n_s. \tag{8}$$

Finally, Kriging model is trained over sampled data by maximizing ln-likelihood function given by

$$l(\theta_k) = -\left[n_s \ln\left(\hat{\sigma}^2\right) + \ln|\mathbf{R}|\right] \Big/ 2, \tag{9}$$

with parameters $\theta_k > 0$, where $\hat{\sigma}^2$ and $|\mathbf{R}|$ are both functions of θ_k. The best estimate of θ_k is obtained by solving the unconstrained optimization problem with global optimizer for maximizing the likelihood function. In this work we have used genetic algorithm, a global search method for maximizing likelihood function.

As mentioned above, Kriging method could result in error when presented with noisy data when more points are included in close proximity to each other. This problem of an approximating a noisy data is solved by adopting a regression Kriging technique which allows Kriging model to regress over data [35]. This is accomplished by adding regularization parameter λ to the diagonal elements of Kriging correlation matrix $\mathbf{R}$, making it $\mathbf{R} + \lambda\mathbf{I}$ for regression Kriging method where $\mathbf{I}$ is an identity matrix. This addition of regularization parameter does not force predictor to pass through sample points and it is evaluated by optimizing maximum likelihood function along with θ_k parameter. The regression Kriging predictor is given by

$$\hat{y}_r(\mathbf{x}_u) = \hat{\beta}_r + \mathbf{r}^{\mathrm{T}}(\mathbf{x}_u)(\mathbf{R} + \lambda\mathbf{I})^{-1}\left(\mathbf{y} - g\hat{\beta}_r\right), \tag{10}$$

where

$$\hat{\beta}_r = (g^{\mathrm{T}}(\mathbf{R} + \lambda\mathbf{I})^{-1}g)^{-1}g^{T}(\mathbf{R} + \lambda\mathbf{I})^{-1}\mathbf{y}, \tag{11}$$

and variance $\hat{\sigma}_r^2$ of regression Kriging model is computed by

$$\hat{\sigma}_r^2 = \frac{\left[\left(y - g\hat{\beta}_r\right)^{\mathrm{T}}(\mathbf{R} + \lambda\mathbf{I})^{-1}\left(y - g\hat{\beta}_r\right)\right]}{n_s}. \tag{12}$$

The subscript "r" in above equations denotes regression. The regression Kriging model is described in detail by Forrester et al. [35].

4.3 Infill criteria

The training of a regression Kriging model with initial sample data provide an approximation of objective function over the whole parametric design space. This metamodel can be further refined by providing more sample data points to the metamodel in design domain based on infill criteria. Each infill point is an additional objective function evaluation supplied to the optimizer to create a refined metamodel. The addition of infill points improves global and local accuracy of the metamodel offering better estimate of global optimum. In every optimization iteration regression Kriging metamodel is constructed based on existing points. The new point then suggested based on infill criteria. Later that point is added to the initial sample and metamodel is rebuilt with augmented data set. This process is followed till metamodel satisfy termination criteria. In this study we will use expected improvement

(EI) as an infill criterion for balance exploration and exploitation of objective function [35]. The EI for regression Kriging is an extension to the EI method for Kriging which uses reinterpolation technique [35] for finding new infill point. The infill point is obtained by maximizing EI improvement function given by

$$E[I(\mathbf{x})] = \begin{cases} (y_{min} - \hat{y})\Phi\left(\frac{(y_{min}-\hat{y}_r)}{\hat{s}}\right) + \hat{s}\phi\left(\frac{(y_{min}-\hat{y}_r)}{\hat{s}}\right), & \hat{s} > 0, \\ 0, & \hat{s} = 0, \end{cases}$$

(13)

where $\Phi()$ and $\phi()$ are normal cumulative distribution function and probability density function. The mean square error of metamodel $\hat{s}^2$ is given by

$$\hat{s}^2 = \hat{\sigma}_{ri}^2 \left[1 - \mathbf{r}^\mathsf{T}\mathbf{R}^{-1}\mathbf{r}\right].$$

(14)

The $\hat{\sigma}_{ri}^2$ is variance of regression Kriging metamodel with reinterpolation technique and it is given by

$$\hat{\sigma}_{ri}^2 = \frac{\left[\left(y - g\hat{\beta}_r\right)^\mathsf{T}(\mathbf{R} + \lambda\mathbf{I})^{-1}\mathbf{R}(\mathbf{R} + \lambda\mathbf{I})^{-1}\left(y - g\hat{\beta}_r\right)\right]}{n_s}.$$

(15)

It should be noted that $\hat{s}$ goes to zero at already sampled points [35] which produces zero EI value. This technique makes sure that existing data point does not resample with infill criteria which makes this infill procedure eventually find the global optimum [41]. The EI method for regression Kriging with reinterpolation technique is described in Forrester et al. [35].

4.4 Termination criteria

It is common to use a preset number of infill points (fixed budget infill process) or overall global accuracy of the metamodel as the termination criteria. Global accuracy of the metamodel refers to how accurately the model can predict the objective function throughout the whole design space and local accuracy refers to how accurately the objective function can be predicted at the optimum point. In this study, a fixed budget of 10 infill points were used. The optimization was terminated when this fixed budget was exceeded or the global error reduced to 2%, whichever happened first. The global accuracy of regression Kriging metamodel is estimated by generating test data sample and evaluating normalized root mean squared error (NRMSE) at test data points. A separate set of 20 data points as per the LHS sampling technique distributed throughout the design space was measured. The metamodel was used to predict the objective function values at these 20 locations. Later the objective function values at

test data are experimentally measured as discussed earlier. Then the NRMSE of the metamodel is estimated by

$$NRMSE = \frac{\sqrt{\frac{\sum_{i=1}^{n_{Test}}\left(F_{Test}^i - F_{Metamodel}^i\right)^2}{n_{Test}}}}{F_{\max(IS)}},$$

(16)

where F_{Test} and $F_{Metamodel}$ represents objective function value of test data sample with experimental evaluation and metamodel prediction respectively. The n_{Test} represents the number of test data samples (20 in this study). The root mean squared error is then normalized with maximum objective function value $F_{\max(IS)}$ of the initial sampling (IS) plan of 24 data points.

5 Results and discussions

5.1 Baseline verification

In the present study, a baseline test case with no plasma actuator mounted around the airfoil leading edge was performed to characterize the aerodynamic performance of the airfoil model at the Reynolds numbers of $Re = 0.2 \times 10^6$ and 0.4×10^6 for the angles of attack between $-2°$ and $30°$ (i.e., $\alpha = -2°$ to $30°$). During the experiments, all the pressure taps were available for surface pressure measurement as no plasma actuator was mounted at the airfoil leading edge. The blockage of the test model at $\alpha = 10°$ was only about 4%. The blockage the highest α tested (i.e., $\alpha = 24°$) is about 10%. The airfoil model spanned the entire test section to avoid any three dimensional effects at the ends of the test model.

The pressure distribution over the surface of the turbine airfoil model were measured every 2° intervals. The measured pressure distributions were integrated to obtain the C_l at the given α's, as depicted in Fig. 5. The C_l values were compared with the measurement results reported previously by other researchers with the test model of same DU-96-W-180 airfoil shape at the Reynolds number of $Re \approx 1.0 \times 10^6$ [20]. It can be seen clearly that, the measured lift coefficients of the present study agree well with those reported in the published work of Timmer and van Rooij [36] until close to the stall point (i.e., $\alpha \approx 10°$). The measured C_l values of the present study were found to be lower than those reported by Timmer and van Rooij [36] at the higher angles of attack beyond the stall point (i.e., $\alpha > 10°$) due to the much higher Reynolds number used in their experiments.

5.2 Sampling points

The sampling points distribution in terms of the design variables used here (i.e., the voltage and frequency) are shown
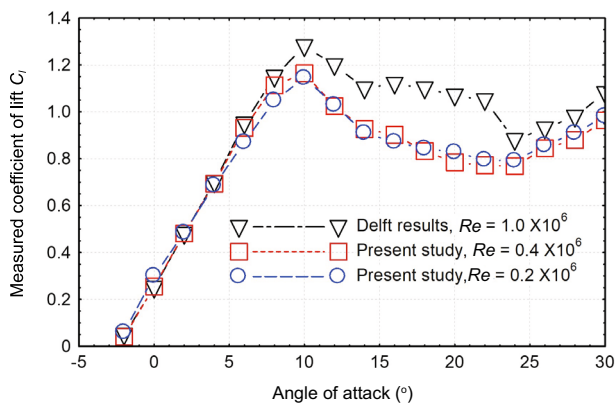
Fig. 5 Measured lift coefficient of DU-96-W-180 airfoil model without plasma actuator
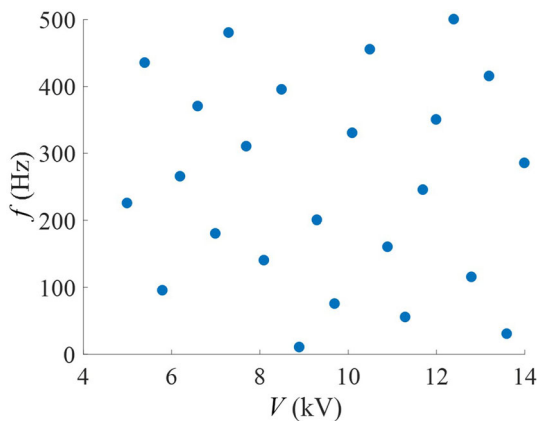

Fig. 6 Distribution of the design variables used in the present study

in Fig. 6. As mentioned earlier, 24 LHS sample data points were used in the present study.

5.3 Pressure measurements with plasma actuator turning on

Rethmel et al. [42] used NS-DBD plasma for flow separation control over a NACA-0015 airfoil surface. They found that the frequency of NS-DBD plasma activation is very critical to the effectiveness of the flow control. Similar to the setup used in the present study, since the plasma actuator was mounted at the leading edge of the airfoil model, some of the pressure taps close to airfoil leading edge were unavailable for the surface pressure measurements. Therefore, the magnitude of pressure coefficient at the nearest measureable point closest to the airfoil leading edge, at different non-dimensional plasma activation frequencies, f^+ were compared. As described in Rethmel et al. [42], the frequency of plasma activation in non-dimensional terms, f^+. Non-dimensional frequency is defend as $f^+ = \frac{fx}{U_\infty}$. In this equation, f is the frequency of applied plasma pulses, x is the distance over the suction surface from the leading edge to
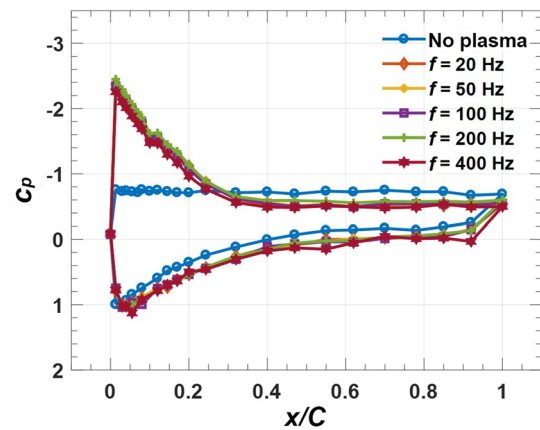

Fig. 7 Measured surface pressure distributions over the turbine airfoil model for some selected frequencies of applied plasma at the Reynolds number of 200×10^3 and $\alpha = 20°$

the point of separation of the flow and U_∞ is the free stream velocity.

It was revealed that for relatively lower α's close to stall, the pressure coefficient was not sensitive to activation frequency. This refers to a condition where the plasma actuator merely acts an active trip and no natural flow instabilities are excited. At higher α, it was found that there was a clear frequency preference where the optimum non-dimensional frequency was reported to be 1.9 ($f^+ = 1.9$) indicating excitation of natural flow instabilities. Zheng et al. [12] reports a similar finding where they categorized the flow control regime into two based on α. The first regime extended from the start of leading edge separation to about 2º past this angle (i.e., $\alpha_{stall} < \alpha < \alpha_{stall} + 2°$). It was observed that within this regime, the plasma actuator merely acts like an active trip where there is no frequency preference. However, for the second regime which is corresponding to higher α's (i.e., $\alpha > \alpha_{stall} + 2°$), the NS-DBD actuator continues providing perturbations and generating spanwise vortices, resulting in a partially reattached flow, i.e., the effect on plasma on flow control could be observed only beyond 2° past leading edge separation. Similar observations were also made in the present study, as shown clearly in Fig. 7.

In the present study, the surface pressure distribution over the surface of the trubine airfoil model was first obtained without switching on the NS-DBD plasma actuator (i.e., passive actuator case) to obtain the baseline for comparison. Then, the NS-DBD plasma actuator was switched on as per the applied voltages and frequencies obtained from the sampling scheme given in Fig. 6. It was found that the airflow would separate almost completely from the entire upper surface starting at the angle of attack of α = 20° without the plasma activation (i.e., the airfoil enters a deep stall state at α = 20° without plasma actuation). As revealed from the measurement results given in Fig. 7, the surface pressure dis-
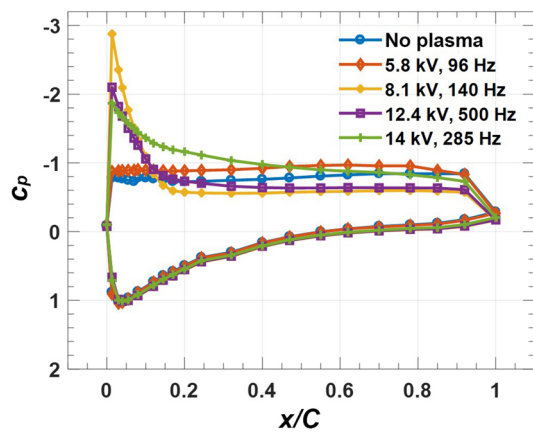
Fig. 8 Measured surface pressure distribution over the airfoil surface for selected sample data points at the Reynolds number of $Re = 300 \times 10^3$ and $\alpha =22°$
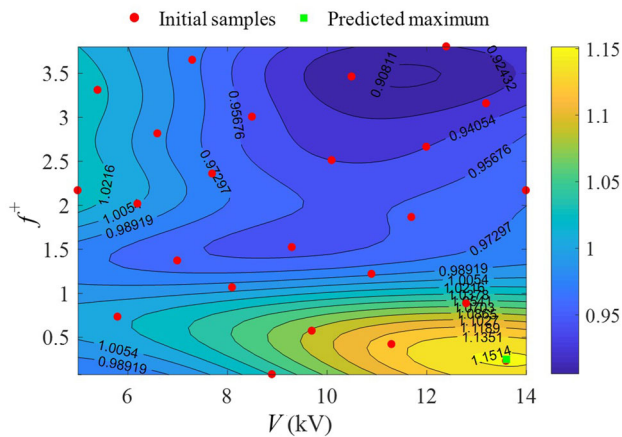

Fig. 9 Predicted lift coefficient contour with the initial sample points ($Re = 200 \times 10^3$ and $\alpha = 24°$)

tribution shows a partial reattachment at $\alpha = 20°$ when the plasma actuator is turned on. But the extent of reattachment does not vary with the frequency of the applied voltage pulses irrespective of voltage. It indicates that no flow instabilities are excited by the plasma actuation, and the plasma actuator would merely act as an active trip. Therefore at α's less than 20°, the plasma actuator was not found to be effective with the setup used in the present study.

For the cases with higher α's, the effectiveness of the plasma actuation for flow separation suppression could be clearly observed. Figure 8 shows a representative plot of five different cases of plasma activation under the experimental conditions of Reynolds number of $Re = 300 \times 10^3$ and $\alpha = 22°$. The no plasma case shows that airfoil is under deep stall. When the NS-DBD plasma actuator was switched on, some combination of the applied voltages and frequencies were found to have less impact on the flow separation control, while some other combinations were found to be have more favorable effects.

5.4 Initial regression Kriging metamodel

The measurement results at $\alpha = 24°$ and Reynolds number of $Re = 200 \times 10^3$ are presented first. As described earlier, the measured surface pressure distribution for each test case was integrated to obtain the total lift forces acting on the airfoil model under the given test conditions (i.e., for the 24 combinations of applied voltage and frequency as in the sampling scheme). The C_l was thereby obtained for each of the sample points. Then, a regression Kriging metamodel was created based on the values of the design variables at the initial 24 samples data points and the corresponding C_l values. A regression Kriging predictor function was then used to predict the C_l throughout the parametric design space. The contour plot of the predicted C_l values is shown in Fig. 9. The initial samples used for creating the metamodel can also be seen on the contour plot. It may be noted the frequency has been expressed in non-dimensional terms f^+.

5.5 Adding infill points

A set of infill points are used to improve the global and local accuracy of the metamodel. Each infill point is an additional value of C_l evaluated at a new sample point at a different combination of input variables (voltage and frequency in this study) suggested by the infill criteria explained earlier. Each infill point was separately added to the metamodel sequentially and a new refined metamodel was created each time with the latest infill point added to the set of sample points already available. i.e., each new metamodel has one additional sample data point compared to the previous one. In order to estimate the global accuracy of the model, a separate set of 20 test data points uniformly distributed across the design space were measured experimentally. The sampling scheme was once again designed based on the Latin hypercube sampling (LHS) technique mentioned earlier. The distribution of the test data points is shown in Fig. 10. The corresponding C_l values obtained from the experiments were compared with the predicted values from the refined metamodel. The NRMSE of the all the sampling points were calculated as explained earlier, and the process of adding infill points was terminated when the fixed budget of 10 infill points was reached. The fixed budget of 10 infill points were used up before the global error reduced to 2%. It was found that the NRMSE was about 2.5% at the end of infill process. But it could be seen that even before the infill process was conducted the NRMSE was reasonably low (about 2.75%) which indicates that regression Kriging technique is well suited for this optimization and the initial number of samples chosen (i.e., 24 samples) is reasonable. The resulting contour plot and NRMSE distribution are shown in Figs. 11 and 12, respectively.
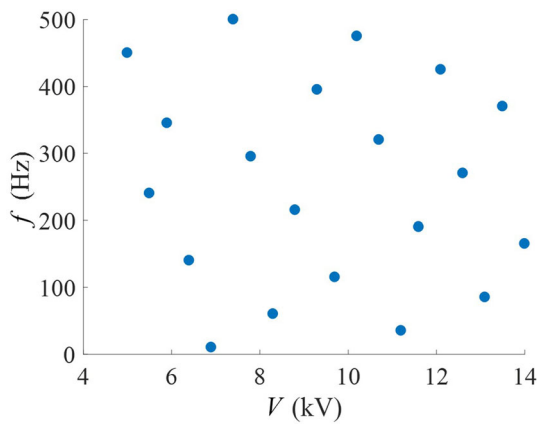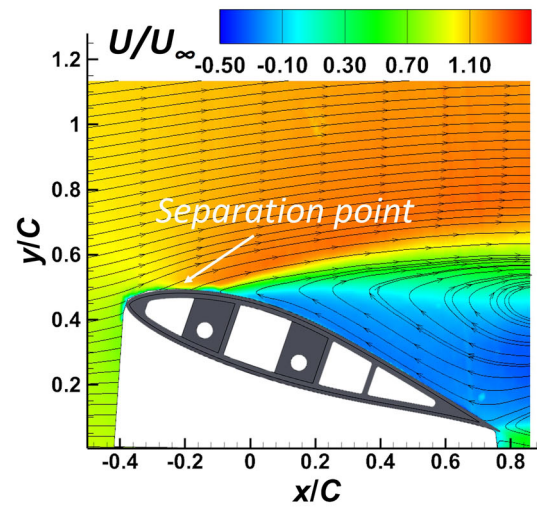
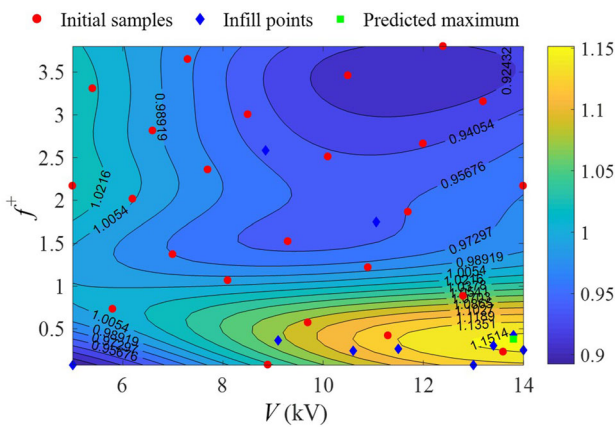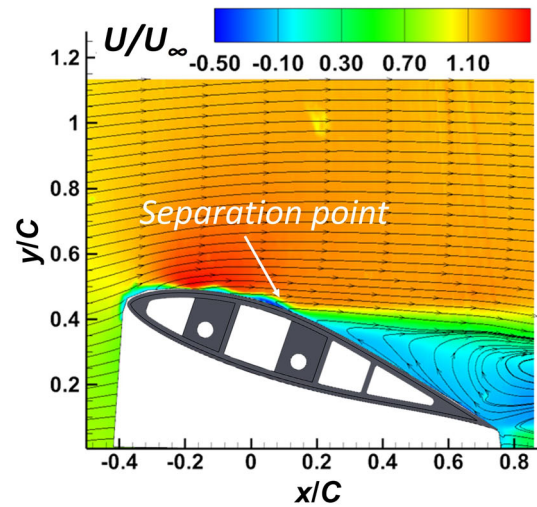Fig. 10 20 test data points used to estimate the global accuracy of the model

Fig. 11 Predicted final lift coefficient contour with the metamodel after infilling process (Reynolds number 200×10^3 and $\alpha = 24°$)
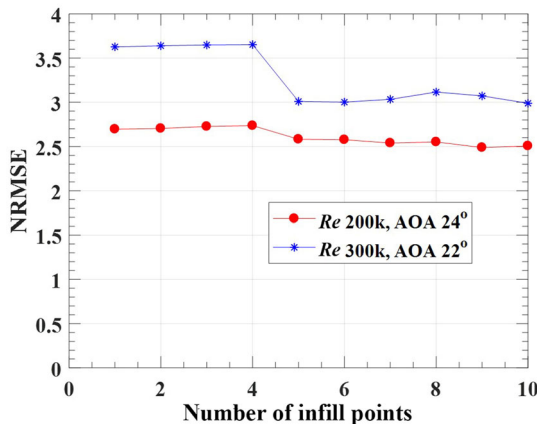
Fig. 12 NRMSE with number of infill points

(a) Before turning on DBD plasma actuation

(b) After turning on DBD plasma actuation

Fig. 13 PIV measurement results to reveal the dramatic changes of the flow characteristics around the airfoil model at AOA $\approx 24°$ before and after turning on the NS-DBD plasma actuator

As described above, a high-resolution digital PIV system was used in the present study to quantify the flow field around the airfoil model in order to reveal the effectiveness of flow separation suppression by using the NS-DBD plasma actuation. Figure 13 gives the ensemble-averaged PIV mea-

surement results for the test cases before and after turning on the NS-DBD plasma actuator. It can be seen clearly that, before turning on the plasma actuator, the airfoil was in deep stall at AOA $\approx 24°$ with massive flow separation over almost the entire airfoil upper surface (i.e., flow separation point locating at very near the airfoil leading edge), as shown in Fig. 3a. As a result, the lift coefficient of the airfoil model would be significantly reduced. However, after the plasma actuator was turned on, the flow separation point over the upper surface of the airfoil model was found to push much further downstream as shown clearly in Fig. 13b, and the flow separation over the front portion of the airfoil model was found to be suppressed effectively. Here, the optimum

combination of the design variables corresponding to $\alpha = 24°$ and $Re = 200 \times 10^3$ have been used to activate the plasma. The applied voltage was 13.8 kV and the f^+ was 0.4.

a. Before turning on DBD plasma actuation.
b. After turning on DBD plasma actuation.

The final metamodel was used to predict the $C_{l\max}$ (objective function). It was found that the $C_{l\max}$ was predicted at a voltage of 13.8 kV and non-dimensional frequency, f^+, of 0.4 as shown in Table 1. The $C_{l\max}$ thus obtained was verified with experiments. It was found that the error in the predicted $C_{l\max}$ was about 2% of the experimentally verified value. The results of the study conducted to verify the dependence of optimum parameters on Reynolds number and α are shown in Figs. 14 and 15. This case corresponds to a different Reynolds number ($Re = 300 \times 10^3$) and $\alpha = 22°$. The same sampling scheme and test parameters were used here as in the previous case. Figure 14 shows the contour plot of the lift coefficients predicted by the regression Kriging metamodel created with only the initial 24 samples. Figure 15 shows the same predicted by the refined metamodel after the infill process. Again, the fixed budget infill points criterion was reached before the NRMSE dropped below 2%. The error in $C_{l\max}$ predicted by this new model was also experimentally verified to be about 2%. The results of both cases are shown in Table 1. Case I corresponds to $\alpha = 24°$ at Reynolds number of 200×10^3 while Case II corresponds to $\alpha = 22°$ at Reynolds number of 300×10^3.

It should be noted that, by comparing the predicted maximum lift coefficient from Figs. 9 and 11 that the optimum parameters before the infill process were V = 13.5 kV and f^+ = 0.25, and after adding the infill points, it was 13.8 kV and 0.4. The difference is more prominent in the case II corresponding to Reynolds number 300×10^3 and $\alpha = 22°$ which indicates that the infill points helps to improve the local accuracy as well as the global accuracy of the model.

It should be pointed out that, there is no common consensus on the optimum f^+ as it is found to be different for different studies. For instance, Zheng et al. [25] conducted experiments on the use of NS-DBD plasma on a NACA 0015 airfoil model at Reynolds number of 468×10^3 and α ranging from 16.5° to 21°. It was found that the optimum forcing frequency (f^+), using the maximum lift coefficient as a performance indicator was around 0.4–0.5. This range was maintained even at a different Reynolds number of $Re = 268 \times 10^3$ over a similar range of α's, indicating that the optimum non-dimensional forcing frequency using a given performance indicator may not vary with α and Reynolds number. However, the study by Rethmel et al. [42] on flow separation control over same airfoil using NS-DBD plasma reported the optimum f^+ to be 1.9. This could be due to different performance indicators used in studies. The former
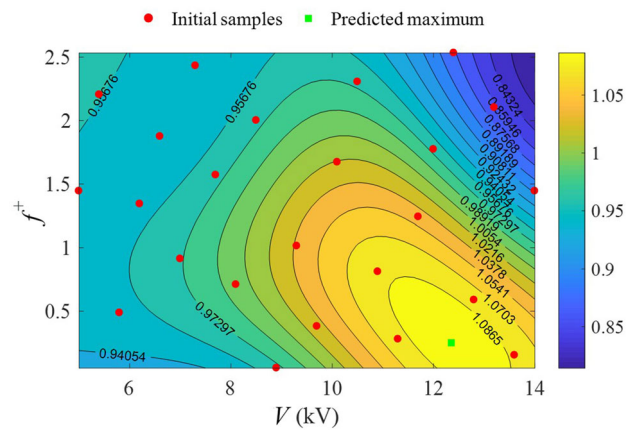

Fig. 14 Predicted lift coefficient contour plot with the initial sample points ($Re = 300 \times 10^3$, $\alpha = 22°$)

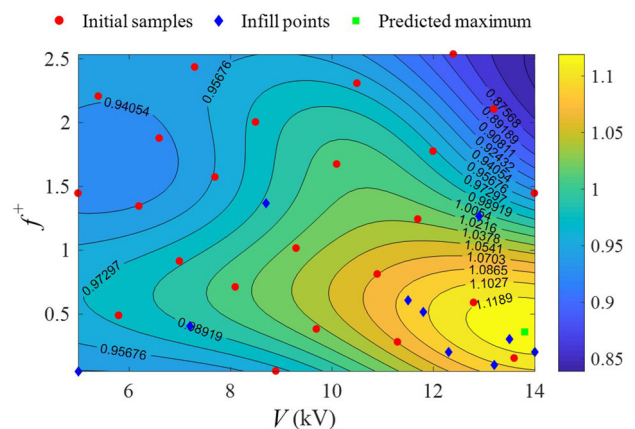Fig. 15 Predicted final lift coefficient contour with the metamodel after infilling process ($Re = 300 \times 10^3$ and $\alpha = 22°$)

study used C_l and the latter study used the pressure coefficient at the nearest measurable point as the performance indicator.

Such parametric evaluations of the objective function using metamodeling techniques over the whole design space could be used for optimizing economics of power production. The average electrical power consumed by the plasma actuator operating in nano-second mode may be estimated from the instantaneous voltage and current measurements as

$$P_{avg} = \frac{1}{t_2 - t_1} \int_{t_1}^{t_2} V(t)I(t)dt, \tag{17}$$

where V is the instantaneous applied voltage in Volts, I is the instantaneous current generated in amperes and t is the time in seconds.

The instantaneous voltage and current were measured using a voltage probe and current probe connected to the oscilloscope. The energy consumed in a single pulse is first

Table 1 Summary of the final results

Parameters	Case I $Re = 200 \times 10^3, \alpha = 24°$	Case II $Re = 300 \times 10^3, \alpha = 22°$	Description
C_l	0.830	0.869	Measured C_l value without NS-DBD Plasma actuation
Predicted $C_{l\max}$	1.169	1.132	Predicted $C_{l\max}$ value (with plasma)
V	13.8	13.8	Predicted voltage (kV)
f^+	0.4	0.4	Predicted actuation Frequency, f^+
Measured $C_{l\max}$	1.145	1.109	Experimentally measured $C_{l\max}$ value
Error	2.10%	2.07%	Relative prediction error
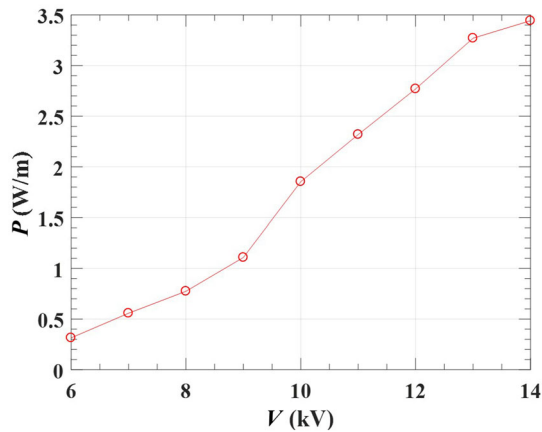
Fig. 16 Power consumed by the plasma actuator as a function of the applied voltage

estimated from the oscilloscope data and it can be converted to electrical power based on number of pulses per second (frequency of plasma). The optimum forcing frequency for Case I in dimensional terms is ~ 50 Hz. Figure 16 shows the electrical power consumed by the plasma actuator as a function of applied voltage for a fixed frequency of 50 Hz. NS-DBD plasma power consumption is a linear function of frequency. The power consumed is expressed in W/m length of the actuator. It may be observed from Fig. 11 that a reduction in voltage from about 14 to 12 kV would reduce the $C_{l\max}$ negligibly (~ 1.5%) whereas from Fig. 14 it could be seen that this would reduce the power consumption from 3.5 to 2.75 W/m which is ~ 20% less electrical power being consumed. Since active flow control continuously consumes energy for operation, having a metamodel which could accurately predict the whole parametric design space could help to achieve a tradeoff between power consumption and economics of power production in large wind farms.

6 Conclusion

While DBD plasma-based approach has been demonstrated recently to be effective to suppress flow separation/airfoil

stall to improve turbine power production performance and mitigate the unsteady wind loadings acting on turbine blades, it is still a non-trivial task to optimize the design variables of a DBD plasma actuation system to maximum its effectiveness for flow control. In the present study, a regression Kriging-based metamodeling technique is employed to optimize the operation parameters of a DBD plasma system to suppress the massive flow separation/airfoil stall over the surface of a wind turbine airfoil model. While most of previous studies on DBD plasma-based flow control varied only one parameter at a time, the present study used a regression Kriging based metamodel approach to explore the whole design space by varying multiple design variables, which could drastically reduce the number of experiments required for the operation parameter optimization.

In the present study, a wind turbine blade section model with DU-96-W-180 airfoil profile in the cross section was designed/manufactured and mounted in a low-speed wind tunnel for an experimental investigation. A DBD plasma actuation system was embedded around the leading edge of the turbine airfoil model in order to demonstrate the use of regression Kriging metamodeling technique for parametric optimization of input parameters. During the experiments, the DBD plasma system was operated in a nanosecond-pulsed plasma actuation mode (i.e., NS-DBD plasma). Two operation parameters (i.e., applied voltage and frequency) for the NS-DBD Plasma actuation were varied simultaneously as per a predefined sampling scheme to create a metamodel. The lift coefficient of the turbine airfoil model at a typical deep stall $\alpha = 24°$ at the Reynolds number level of $Re = 200 \times 10^3$ was chosen as the objective function to be optimized. The surface pressure distribution over the airfoil model was measured and integrated to obtain the lift coefficient of the airfoil model at the selected sample points. The data set served as the evaluations of the objective function at the sample points to be fed to the metamodel. An initial regression Kriging metamodel was created which was further improved by adding infill points to create the final refined model. A metamodel trained prediction function was then established to predict the lift coefficient of the airfoil model throughout the whole two-dimensional design space.

The final value of the lift coefficient of the airfoil model predicted via the metamodeling was experimentally verified, and the error was found to be about 2.0%. The global error of the metamodel within the entire design space were found to be about 3.0%. The procedure was also repeated at $\alpha = 22°$ at the Reynolds number of $Re = 300 \times 10^3$ to verify the sensitivity of the optimum parameters to the Reynolds number and α. It was demonstrated successfully that the Metamodeling-based optimization technique would save the cost of extensive experimentation required to explore the whole design space by performing experiments only at sample locations, yet without much loss in accuracy.

References

1. Wiser, R., Lantz, E., Mai, T., et al.: Wind vision: a new era for wind power in the United States. Electr. J. **28**, 120–132 (2015). https://doi.org/10.1016/j.tej.2015.09.016

2. Sun, H., Luo, Y., Zhao, Z., et al.: The impacts of Chinese wind farms on climate. J. Geophys. Res. **123**, 5177–5187 (2018). https://doi.org/10.1029/2017JD028028

3. Shun, S., Ahmed, N.A.: Wind turbine performance improvements using active flow control techniques. Proc. Eng. **49**, 83–91 (2012). https://doi.org/10.1016/j.proeng.2012.10.115

4. Meijerink, J.A.W., Hoeijmakersy, H.W.M.: Plasma actuators for active flow control on wind turbine blades. In: 29th AIAA applied aerodynamics conference, March (2011). https://doi.org/10.2514/6.2011-3353

5. Tian, W., Ozbay, A., Wang, X.D., et al.: Experimental investigation on the wake interference among wind turbines sited in atmospheric boundary layer winds. Acta. Mech. Sin. **33**, 742–753 (2017). https://doi.org/10.1007/s10409-017-0684-5

6. Gad-el-Hak, M.: Flow Control: Passive, Active, and Reactive Flow Management. Cambridge University Press, Cambridge (2007)

7. van Dam, C.P., Chow, R., Zayas, J.R., et al.: Computational investigations of small deploying tabs and flaps for aerodynamic load control. J Phys (2007). https://doi.org/10.1088/1742-6596/75/1/012027

8. Nelson, R.C., Corke, T.C., Othman, H., et al.: A smart wind turbine blade using distributed plasma actuators for improved performance. In: 46th Aerospace Sciences Meeting, January 7–10 (2008). https://doi.org/10.2514/6.2008-1312

9. Roth, J., Sherman, D., Wilkinson, S.: Boundary layer flow control with a one atmosphere uniform glow discharge surface plasma. In: 36th AIAA Aerospace Sciences Meeting and Exhibit (1998). https://doi.org/10.2514/6.1998-328

10. Corke, T.C., Post, M.L., Orlov, D.M.: Single dielectric barrier discharge plasma enhanced aerodynamics: physics, modeling and applications. Exp. Fluids **46**, 1–26 (2009). https://doi.org/10.1007/s00348-008-0582-5

11. Roupassov, D.V., Nikipelov, A.A., Nudnova, M.M., et al.: Flow separation control by plasma actuator with nanosecond pulsed-periodic discharge. AIAA J. **47**, 168–185 (2009). https://doi.org/10.2514/1.38113

12. Zheng, J.G., Cui, Y.D., Zhao, Z.J., et al.: Investigation of airfoil leading edge separation control with nanosecond plasma actuator. Phys. Rev. Fluids **1**, 1–30 (2016). https://doi.org/10.1103/PhysRevFluids.1.073501

13. Dawson, R., Little, J.: Characterization of nanosecond pulse driven dielectric barrier discharge plasma actuators for aerodynamic flow control. J. Appl. Phys. **113**, 103302 (2013). https://doi.org/10.1063/1.4794507

14. Moreau, E.: Airflow control by non-thermal plasma actuators. J. Phys. D Appl. Phys. **40**, 605–636 (2007). https://doi.org/10.1088/0022-3727/40/3/S01

15. Forte, M., Jolibois, J., Pons, J., et al.: Optimization of a dielectric barrier discharge actuator by stationary and non-stationary measurements of the induced flow velocity: application to airflow control. Exp. Fluids **43**, 917–928 (2007). https://doi.org/10.1007/s00348-007-0362-7

16. Corke, T.C., Enloe, C.L., Wilkinson, S.P.: Dielectric barrier discharge plasma actuators for flow control. Annu. Rev. Fluid Mech. **42**, 505–529 (2010). https://doi.org/10.1146/annurev-fluid-121108-145550

17. Hikaru, A., Hiroaki, F., Yoshiaki, A., et al.: Separated flow control of small horizontal-axis wind turbine blades using dielectric barrier discharge plasma actuators. Energies **13**, 1218 (2020). https://doi.org/10.3390/en13051218

18. Chen, K., Wei, C.Y., Shi, Z.W.: Effect of NS-DBD actuator parameters on the aerodynamic performance of a flap lifting device. Appl. Sci. (Switzerland) **9**, 5161 (2019). https://doi.org/10.3390/app9235213

19. Wei, B., Wu, Y., Liang, H., et al.: Flow control on a high-lift wing with microsecond pulsed surface dielectric barrier discharge actuator. Aerosp. Sci. Technol. **96**, 105584 (2020). https://doi.org/10.1016/j.ast.2019.105584

20. De Giorgi, M.G., Motta, V., Suma, A.: Influence of actuation parameters of multi-DBD plasma actuators on the static and dynamic behaviour of an airfoil in unsteady flow. Aerosp. Sci. Technol. **96**, 105587 (2020). https://doi.org/10.1016/j.ast.2019.105587

21. Yu, H., Zheng, J.: Numerical investigation of control of dynamic stall over a NACA0015 airfoil using dielectric barrier discharge plasma actuators. Phys. Fluids **32**, 35103 (2020). https://doi.org/10.1063/1.5142465

22. Goyagi, R., Komuro, A., Kawate, R., et al.: Surface pressure modification driven by a dielectric-barrier-discharge plasma actuator: performance dependence on airfoil shape. AIP Adv. **10**, 35311 (2020). https://doi.org/10.1063/1.5141364

23. Little, J., Takashima, K., Nishihara, M., et al.: Separation control with nanosecond-pulse-driven dielectric barrier discharge plasma actuators. AIAA J. **50**, 350–365 (2012). https://doi.org/10.2514/1.J051114

24. Reece Roth, J., Dai, X.: optimization of the aerodynamic plasma actuator as an electrohydrodynamic (EHD) electrical device. In: Collection of Technical Papers—44th AIAA Aerospace Sciences Meeting 19, 14604–14631 (2006). https://doi.org/10.2514/6.2006-1203

25. Zheng, J., Cui, Y.D., Zhao, Z., et al.: flow separation control over a NACA 0015 airfoil using nanosecond-pulsed plasma actuator. AIAA J. **56**, 2220–2234 (2018). https://doi.org/10.2514/1.J056111

26. Hikaru, A., Taku, N., Aiko, Y., et al.: Plasma flow control simulation of an airfoil of wind turbine at an intermediate Reynolds number. In: ASME 2013 Fluids Engineering Division Summer Meeting. American Society of Mechanical Engineers, 1–10 (2013). https://doi.org/10.1115/fedsm2013-16327

27. Simpson, T.W., Mauery, T.M., Korte, J.J., et al.: Kriging models for global approximation in simulation-based multidisciplinary design optimization. AIAA J. **39**, 2233–2241 (2001)

28. Queipo, N.V., Haftka, R.T., Shyy, W., et al.: surrogate-based analysis and optimization. Prog. Aerosp. Sci. **41**, 1–28 (2005). https://doi.org/10.1016/j.paerosci.2005.02.001

29. Booker, A., Frank, P.D., Serafini, D.B.: Optimization using surrogate objectives on a helicopter test example. Springer (1998). https://doi.org/10.1007/978-1-4612-1780-0_3

30. Mason, W.H., Watson, L.T., Grossman, B., et al.: response surface models combining linear and Euler aerodynamics for supersonic transport design. J. Aircraft **36**, 75–86 (2008). https://doi.org/10.2514/2.2415

31. Madavan, N.K., Rai, M.M., Huber, F.W.: Neural net-based redesign of transonic turbines for improved unsteady aerodynanamic performance. https://ntrs.nasa.gov/archive/nasa/casi.ntrs.nasa.gov/19990008889.pdf

32. Madsen, J.I., Shyy, W., Haftka, R.T.: response surface techniques for diffuser shape optimization. AIAA J. **38**, 1512–1518 (2012). https://doi.org/10.2514/3.14576

33. Papila, N., Shyy, W., Griffin, L., et al.: Shape optimization of supersonic turbines using global approximation methods. J. Propul. Power **18**, 509–518 (2008). https://doi.org/10.2514/2.5991

34. Shyy, W., Papila, N., Vaidyanathan, R., et al.: global design optimization for aerodynamics and rocket propulsion components. Prog. Aerosp. Sci. **37**, 59–118 (2001). https://doi.org/10.1016/S0376-0421(01)00002-1

35. Forrester, A.I.J., Keane, A.J., Bressloff, N.W.: Design and analysis of 'noisy' computer experiments. AIAA J. **44**, 2331–2339 (2006). https://doi.org/10.2514/1.20068

36. Timmer, W.A., Rooij, R.: Summary of the Delft university wind turbine dedicated airfoils. J. Sol. Energy Eng. **125**, 488 (2003). https://doi.org/10.1115/1.1626129

37. McKay, M.D., Beckman, R.J., Conover, W.J.: A comparison of three methods for selecting values of input variables in the analysis of output from a computer code. Technometrics **42**, 55–61 (2000). https://doi.org/10.1080/00401706.2000.10485979

38. Morris, M.D., Mitchell, T.J.: Exploratory designs for computational experiments. J. Stat. Plan. Inferen. **43**, 381–402 (1995). https://doi.org/10.1016/0378-3758(94)00035-T

39. Krige, D.G.: A statistical approach to some basic mine valuation problems on the Witwatersrand. J. South Afr. Inst. Min. Metall. **52**, 119–139 (1951)

40. Matheron, G.: Principles of geostatistics. Econ. Geol. **58**, 1246–1266 (1963). https://doi.org/10.2113/gsecongeo.58.8.1246

41. Forrester, A., Sobester, A., Keane, A.: Engineering Design via Surrogate Modelling: A Practical Guide. Wiley, New York (2008)

42. Rethmel, C., Little, J., Takashima, K., et al.: Flow separation control over an airfoil with nanosecond pulse driven DBD plasma actuators. In: 49th AIAA Aerospace Sciences Meeting including the New Horizons Forum and Aerospace Exposition, January 1–17 (2011). https://doi.org/10.2514/6.2011-487